Numerical simulation and benchmarking of a monolithic multigrid solver for fluid-structure interaction problems with application to hemodynamics

S. Turek, J. Hron, M. Mádlík, M. Razzaq, H. Wobker, and J. F. Acker

Abstract An Arbitrary Lagrangian-Eulerian (ALE) formulation is applied in a fully coupled monolithic way, considering the fluid-structure interaction (FSI) problem as one continuum. The mathematical description and the numerical schemes are designed in such a way that general constitutive relations (which are realistic for biomechanics applications) for the fluid as well as for the structural part can be easily incorporated. We utilize the LBB-stable finite element pairs Q_2P_1 and $P_2^+P_1$ for discretization in space to gain high accuracy and perform as time-stepping the 2nd order Crank-Nicholson, respectively, a new modified Fractional-Step-θ-scheme for both solid and fluid parts. The resulting discretized nonlinear algebraic system is solved by a Newton method which approximates the Jacobian matrices by a divided differences approach, and the resulting linear systems are solved by direct or iterative solvers, preferably of Krylov-multigrid type.
For validation and evaluation of the accuracy and performance of the proposed methodology, we present corresponding results for a new set of FSI benchmark configurations which describe the self-induced elastic deformation of a beam attached to a cylinder in laminar channel flow, allowing stationary as well as periodically oscillating deformations. Then, as an example of FSI in biomedical problems, the influence of endovascular stent implantation on cerebral aneurysm hemodynamics is numerically investigated. The aim is to study the interaction of the elastic walls of the aneurysm with the geometrical shape of the implanted stent structure for prototypical 2D configurations. This study can be seen as a basic step towards the understanding of the resulting complex flow phenomena so that in future aneurysm rupture shall be suppressed by an optimal setting of the implanted stent geometry.

S. Turek, M. Razzaq, H. Wobker, J. F. Acker
Institute for Applied Mathematics, TU Dortmund, Vogelpothsweg 87, 44227 Dortmund, Germany
e-mail: stefan.turek@mathematik.tu-dortmund.de

J. Hron, M. Mádlík
Mathematical Institute, Charles University Prague, Sokolovska 83, 18675 Prague, Czech republic
e-mail: hron@karlin.mff.cuni.cz

1 Introduction

In this paper, we consider the general problem of viscous flow interacting with an elastic body which is being deformed by the fluid action. Such a problem is of great importance in many real life applications, typical examples are the areas of biomedical fluids which include the influence of hemodynamic factors in blood vessels, cerebral aneurysm hemodynamics, joint lubrication and deformable cartilage, and blood flow interaction with elastic veins [2, 9, 25, 26, 34]. The theoretical investigation of fluid-structure interaction problems is complicated by the need of a mixed description for both parts: While for the solid part the natural view is the material (Lagrangian) description, for the fluid it is usually the spatial (Eulerian) description. In the case of their combination some kind of mixed description (usually referred to as the Arbitrary Lagrangian-Eulerian description or ALE) has to be used which brings additional nonlinearity into the resulting equations (see [17]).

The numerical solution of the resulting equations of the fluid-structure interaction problem poses great challenges since it includes the features of structural mechanics, fluid dynamics, and their coupling. The most straightforward solution strategy, mostly used in the available software packages (see for instance [16]), is to decouple the problem into the fluid part and solid part, for each of those parts using some well established solution method; then the interaction process is introduced as external boundary conditions in each of the subproblems. This has the advantage that there are many well tested numerical methods for both separate problems of fluid flow and elastic deformation, while on the other hand the treatment of the interface and the interaction is problematic due to high stiffness and sensitivity. In contrast, the monolithic approach discussed here treats the problem as a single continuum with the coupling automatically taken care of as internal interface. This on the other hand requires more robust nonlinear and linear solvers for the global problem.

Besides a short description of the underlying numerical aspects regarding discretization and solution procedure for this monolithic approach (see [17, 24]), we present corresponding results for a set of FSI benchmarking test cases (‘channel flow around cylinder with attached elastic beam’, see [30]), and we concentrate on prototypical numerical studies for 2D aneurysm configurations and first steps towards full 3D models. The corresponding parameterization is based on abstractions of biomedical data (i.e., cutplanes of 3D specimens from New Zealand white rabbits as well as computer tomographic and magnetic resonance imaging data of human neurocrania). In our studies, we allow the walls of the aneurysm to be elastic and hence deforming with the flow field in the vessel. Moreover, we examine several configurations for stent geometries which clearly influence the flow behavior inside the aneurysm such that a very different elastic displacement of the walls is observed, too. We demonstrate that both the elastic modeling of the aneurysm walls as well as the proper description of the geometrical details of the shape of the aneurysm and particularly of the stents are of great importance for a quantitative analysis of the complex interaction between structure and fluid. This is especially true in view of more realistic blood flow models and anisotropic constitutive laws for the elastic walls.

2 Fluid-structure interaction problem formulation

The general fluid-structure interaction problem consists of the description of the fluid and solid parts, appropriate interface conditions at the interface and conditions for the remaining boundaries, respectively. Here, we consider the flow of an incompressible Newtonian fluid interacting with an elastic solid. We denote the domain occupied by the fluid by Ω_t^f and the solid part by Ω_t^s at the time $t \in [0,T]$. Let $\Gamma_t^0 = \bar{\Omega}_t^f \cap \bar{\Omega}_t^s$ be the part of the boundary where the elastic solid interacts with the fluid. In the following, the description for both fields and the interface conditions are introduced. Furthermore, discretization aspects and computational methods are described.

2.1 Fluid mechanics

The fluid flow is assumed to be laminar. It can be described by the Navier-Stokes equations for incompressible flows

$$\rho^f(\frac{\partial \mathbf{v}^f}{\partial t} + \mathbf{v}\cdot\nabla\mathbf{v}) - \nabla\cdot\sigma^f = \mathbf{0}, \quad \nabla\cdot\mathbf{v} = \mathbf{0} \quad \text{in} \quad \Omega_t^f \tag{1}$$

where ρ^f is the constant density. The state of the flow is described by the velocity and pressure fields $\mathbf{v}^f$, p^f, respectively. The external forces, for example due to gravity or human motion, are assumed to be not significant and are neglected. Although the blood is known to be non-Newtonian in general, we assume it to be Newtonian in this study. This is because we consider large arteries with radii of more than 2 mm, where the velocity and shear rate are high and the kinematic viscosity ν^f is nearly constant [20], such that the non-Newtonian effects can be neglected. The constitutive relation for the stress tensor reads

$$\sigma^f = -p^f\mathsf{I} + 2\mu\mathsf{D}(\mathbf{v}^f), \tag{2}$$

where μ is the dynamic viscosity of the fluid, p^f is the Lagrange multiplier corresponding to the incompressibility constraint in (1), and $\mathsf{D}(\mathbf{v}^f)$ is the strain-rate tensor:

$$\mathsf{D}(\mathbf{v}^f) = \frac{1}{2}(\nabla\mathbf{v}^f + (\nabla\mathbf{v}^f)^T). \tag{3}$$

For the fluid-structure interaction we use the ALE form of the balance equations. The corresponding discretization techniques are discussed in section 3. Let us remark that also non-Newtonian flow models can be used for modeling blood flow, for instance of Power Law type or even including viscoelastic effects (see [7]) which is planned for future extensions.

2.2 Structural mechanics

The governing equations for the structural mechanics are the balance equations

$$\rho^s(\frac{\partial \mathbf{v}^s}{\partial t} + (\nabla \mathbf{v}^s)\mathbf{v}^s - \mathbf{g}) - \nabla \cdot \sigma^s = \mathbf{0}, \quad \text{in} \quad \Omega_t^s, \tag{4}$$

where the superscript s denotes the structure, ρ^s is the density of the material, $\mathbf{g}^s$ represents the external body forces acting on the structure, and σ^s is the Cauchy stress tensor. The deformation of the structure is described by the displacement $\mathbf{u}^s$, with velocity field $\mathbf{v}^s = \frac{\partial \mathbf{u}^s}{\partial t}$. Written in the more common Lagrangian description, i.e. with respect to some fixed reference (for example initial) state Ω^s, we have

$$\rho_0^s(\frac{\partial^2 \mathbf{u}^s}{\partial t^2} - \mathbf{g}) - \nabla \cdot \Sigma^s = \mathbf{0}, \quad \text{in} \quad \Omega^s, \tag{5}$$

where $\Sigma^s = J\sigma^s \mathsf{F}^{-T}$ is the first Piola-Kirchhoff stress tensor. J denotes the determinant of the deformation gradient tensor F, defined as $\mathsf{F} = \mathsf{I} + \nabla \mathbf{u}^s$. Unlike the Cauchy stress tensor σ^s, Σ^s is non-symmetric. Since constitutive relations are often expressed in terms of symmetric stress tensor, it is natural to introduce the second Piola-Kirchhoff tensor S^s

$$\mathsf{S}^s = \mathsf{F}^{-T}\Sigma^s = J\mathsf{F}^{-1}\sigma^s\mathsf{F}^{-T}, \tag{6}$$

which is symmetric. For elastic material the stress is a function of the deformation (and possibly of thermodynamic variables such as the temperature) but it is independent of deformation history and thus of time. The material characteristics may still vary in space. In a homogeneous material mechanical properties do not vary, the strain energy function depends only on the deformation. A material is mechanically isotropic if its response to deformation is the same in all directions. The constitutive equation is then a function of F. More precisely, it is usually written in terms of the Green-Lagrange strain tensor, as

$$\mathsf{E} = \frac{1}{2}(\mathsf{C} - \mathsf{I}), \tag{7}$$

where I is the identity tensor and $\mathsf{C} = \mathsf{F}^T\mathsf{F}$ is the left Cauchy-Green strain tensor.

For the subsequent FSI benchmark calculations we employ the St. Venant-Kirchhoff material model as an example for homogeneous isotropic material whose reference configuration is the natural state (i.e. where the Cauchy stress tensor is zero everywhere). The St. Venant-Kirchhoff material model is specified by the following constitutive law

$$\sigma^s = \frac{1}{J}\mathsf{F}(\lambda^s(\mathrm{tr}\,\mathsf{E})\mathsf{I} + 2\mu^s\mathsf{E})\mathsf{F}^T \qquad \mathsf{S}^s = \lambda^s(\mathrm{tr}\,\mathsf{E})\mathsf{I} + 2\mu^s\mathsf{E}, \tag{8}$$

where λ^s denotes the first Lamé coefficient, and μ^s the shear modulus. More complex constitutive relations for hyperelastic materials may be found in [14], and particular models for biological tissues and blood vessels are reported in [11, 15]. The material elasticity is characterized by a set of two parameters, the Poisson ratio ν^s and the Young modulus E. These parameters satisfy the relations

$$\nu^s = \frac{\lambda^s}{2(\lambda^s + \mu^s)} \qquad E = \frac{\mu^s(3\lambda^s + 2\mu^2)}{(\lambda^s + \mu^s)} \tag{9}$$

$$\mu^s = \frac{E}{2(1+\nu^s)} \quad \lambda^s = \frac{\nu^s E}{(1+\nu^s)(1-2\nu^s)}, \tag{10}$$

where $\nu^s = 1/2$ for incompressible and $\nu^s < 1/2$ for compressible material. In the large deformation case it is common to describe the constitutive equation using a stress-strain relation based on the Green Lagrange strain tensor E and the second Piola-Kirchhoff stress tensor $\mathsf{S}(\mathsf{E})$ as a function of E. However, also incompressible materials can be handled in the same way (see [17]).

For the hemodynamic applications, a Neo-Hooke material model is taken which can be used for compressible or incompressible (for $\nu^s \to 1/2 \Rightarrow \lambda^s \to \infty$) material and which is described by the constitutive laws:

$$\sigma^s = -p^s \mathsf{I} + \frac{\mu^s}{J}(\mathsf{F}\mathsf{F}^T - \mathsf{I}) \tag{11}$$

$$0 = -p^s + \frac{\lambda^s}{2}(J - \frac{1}{J}) \tag{12}$$

Both models, the St. Venant-Kirchhoff and the Neo-Hooke material model, share the isotropic and homogenous properties, and both can be used for the computation of large deformations. However, the St. Venant-Kirchhoff model does not allow for large strain computation, while the Neo-Hooke model is also valid for large strains. In the case of small strains and small deformations, both material laws yield the same linearized material model. We implemented the St. Venant-Kirchhoff material model as the standard model for the compressible case, since the setup of the benchmark does not involve large strains in the oscillating beam structure. Its implementation is simpler and, therefore, the FSI benchmark will hopefully be adopted by a wider group of researchers. If someone wants or has to use the Neo-Hooke material, the results for a given set of E and ν or λ and μ are comparable, if the standard Neo-Hooke material model as in (11), (12) is used. Similarly as in the case of more complex blood flow models, also more realistic constitutive relations for the anisotropic behavior of the walls of aneurysms can be included which however is beyond the scope of this paper.

2.3 Interaction conditions

The boundary conditions on the fluid-solid interface are assumed to be

$$\sigma^f \mathbf{n} = \sigma^s \mathbf{n}, \quad \mathbf{v}^f = \mathbf{v}^s, \quad \text{on} \quad \Gamma_t^0, \tag{13}$$

where $\mathbf{n}$ is a unit normal vector to the interface Γ_t^0. This implies the no-slip condition for the flow and that the forces on the interface are in balance.

3 Discretization and solution techniques

For the moment, we restrict our considerations to two dimensions which allows systematic tests of the proposed methods for biomedical applications in a very efficient way such that the qualitatitive behavior can be carefully analyzed. The corresponding fully implicit, monolithic treatment of the fluid-structure interaction problem suggests that an A-stable second order time stepping scheme and that the same finite elements for both the solid part and the fluid region should be utilized. Moreover, to handle the fluid incompressibility constraints, we have to choose a stable finite element pair. For that reason, the conforming biquadratic, discontinuous linear Q_2P_1 pair is used. Let us define the usual finite dimensional spaces U for displacement, V for velocity, P for pressure approximation as follows

$$\begin{aligned}
U &= \{\mathbf{u} \in L^\infty(I,[W^{1,2}(\Omega)]^2), \mathbf{u} = \mathbf{0} \text{ on } \partial\Omega\},\\
V &= \{\mathbf{v} \in L^2(I,[W^{1,2}(\Omega_t)]^2) \cap L^\infty(I,[L^2(\Omega_t)]^2), \mathbf{v} = \mathbf{0} \text{ on } \partial\Omega\},\\
P &= \{p \in L^2(I,L^2(\Omega))\}.
\end{aligned}$$

Then the variational formulation of the fluid-structure interaction problem is to find $(\mathbf{u},\mathbf{v},p) \in U \times V \times P$ that satisfy the corresponding weak form of the balance equations including appropriate initial conditions. The spaces U,V,P on an interval $[t^n,t^{n+1}]$ would be approximated in the case of the Q_2,P_1 pair as

$$\begin{aligned}
U_h &= \{\mathbf{u}_h \in [C(\Omega_h)]^2, \mathbf{u}_h|_T \in [Q_2(T)]^2 \quad \forall T \in \mathscr{T}_h, \mathbf{u}_h = \mathbf{0} \text{ on } \partial\Omega_h\},\\
V_h &= \{\mathbf{v}_h \in [C(\Omega_h)]^2, \mathbf{v}_h|_T \in [Q_2(T)]^2 \quad \forall T \in \mathscr{T}_h, \mathbf{v}_h = \mathbf{0} \text{ on } \partial\Omega_h\},\\
P_h &= \{p_h \in L^2(\Omega_h), p_h|_T \in P_1(T) \quad \forall T \in \mathscr{T}_h\}.
\end{aligned}$$

Let us denote by $\mathbf{u}_h^n$ the approximation of $\mathbf{u}(t^n)$, $\mathbf{v}_h^n$ the approximation of $\mathbf{v}(t^n)$ and p_h^n the approximation of $p(t^n)$. Consider for each $T \in \mathscr{T}_h$ the bilinear transformation $\psi_T : \hat{T} \to T$, where $\hat{T}$ is the unit square. Then, $Q_2(T)$ is defined as

$$\mathrm{Q}_2(T) = \left\{q \circ \psi_T^{-1} : q \in \text{span} < 1,x,y,xy,x^2,y^2,x^2y,y^2x,x^2y^2 > \right\} \tag{14}$$

with nine local degrees of freedom located at the vertices, midpoints of the edges and in the center of the quadrilateral. The space $P_1(T)$ consists of linear functions defined by

$$\mathrm{P}_1(T) = \left\{ q \circ \psi_T^{-1} : q \in \mathrm{span} < 1, x, y > \right\} \tag{15}$$

with the function value and both partial derivatives located in the center of the quadrilateral, as its three local degrees of freedom, which leads to a discontinuous pressure. The inf-sup condition is satisfied (see [5]); however, the combination of the bilinear transformation ψ with a linear function on the reference square $P_1(\widehat{T})$ would imply that the basis on the reference square did not contain the full basis. So, the method can at most be first order accurate on general meshes (see [3, 5])

$$\|p - p_h\|_0 = O(h). \tag{16}$$

The standard remedy is to consider a local coordinate system (ξ, η) obtained by joining the midpoints of the opposing faces of T (see [3, 22, 29]). Then, we set on each element T

$$P_1(T) := \mathrm{span} < 1, \xi, \eta > . \tag{17}$$

For this case, the inf-sup condition is also satisfied and the second order approximation is recovered for the pressure as well as for the velocity gradient (see [5, 13])

$$\|p - p_h\|_0 = O(h^2) \quad \text{and} \quad \|\nabla(\mathbf{u} - \mathbf{u}_h)\|_0 = O(h^2). \tag{18}$$

For a smooth solution, the approximation error for the velocity in the L_2-norm is of order $O(h^3)$ which can easily be demonstrated for prescribed polynomials or for smooth data on appropriate domains.

In the last section we present first results for 3-dimensional computation where we use the $P_2^+P_1$ pair which also satisfies the Babuška–Brezzi stability condition and yields a stable discretization of the incompressible problems (see [10]).

3.1 Time discretization

In view of a more compact presentation, the applied time discretization approach is described only for the fluid part (see [23] for more details). In the following, we restrict to the (standard) incompressible Navier-Stokes equations

$$\mathbf{v}_t - \nu \Delta \mathbf{v} + \mathbf{v} \cdot \nabla \mathbf{v} + \nabla p = \mathbf{f}, \quad \nabla \cdot \mathbf{v} = 0, \quad \text{in} \quad \Omega \times (0, T], \tag{19}$$

for given force $\mathbf{f}$ and viscosity ν, with prescribed boundary values on the boundary $\partial\Omega$ and an initial condition at $t = 0$.

3.1.1 Basic-θ-scheme

The basic θ-scheme for time discretization reads:

Given $\mathbf{v}^n$ and $\Delta t = t_{n+1} - t_n$, then solve for $\mathbf{v} = \mathbf{v}^{n+1}$ and $p = p^{n+1}$

$$\frac{\mathbf{v} - \mathbf{v}^n}{\Delta t} + \theta[-\nu\Delta\mathbf{v} + \mathbf{v}\cdot\nabla\mathbf{v}] + \nabla p = \mathbf{g}^{n+1}, \quad \mathrm{div}\,\mathbf{v} = 0, \quad \text{in} \quad \Omega \tag{20}$$

with right hand side $\mathbf{g}^{n+1} := \theta\mathbf{f}^{n+1} + (1-\theta)\mathbf{f}^n - (1-\theta)[-\nu\Delta\mathbf{v}^n + \mathbf{v}^n\cdot\nabla\mathbf{v}^n]$. The parameter θ has to be chosen depending on the time-stepping scheme, e.g., $\theta = 1$ for the Backward Euler (BE), or $\theta = 1/2$ for the Crank-Nicholson-scheme (CN) which we prefer. The pressure term $\nabla p = \nabla p^{n+1}$ may be replaced by $\theta\nabla p^{n+1} + (1-\theta)\nabla p^n$, but with appropriate postprocessing, both strategies lead to solutions of the same accuracy. In all cases, we end up with the task of solving, at each time step, a nonlinear saddle point problem of given type which has then to be discretized in space as described above.

These two methods, CN and BE, belong to the group of *One-Step-θ-schemes*. The CN scheme can occasionally suffer from numerical instabilities because of its only weak damping property (not strongly A-stable), while the BE-scheme is of first order accuracy only (however: it is a good candidate for steady-state simulations). Another method which has proven to have the potential to excel in this competition is the Fractional-Step-θ-scheme (FS). It uses three different values for θ and for the time step Δt at each time level. In [24, 31] we additionally introduced a modified Fractional-Step-θ-scheme which particularly for fluid-structure interaction problems seems to be advantageous. A brief description is given below and a detailed description will appear in the thesis [23].

In the following, we use the more compact form for the diffusive and advective part:

$$N(\mathbf{v})\mathbf{v} = -\nu\Delta\mathbf{v} + \mathbf{v}\cdot\nabla\mathbf{v} \tag{21}$$

3.1.2 Fractional-Step-θ-scheme

For the Fractional-Step-θ-scheme we proceed as follows. Choosing $\theta = 1 - \frac{\sqrt{2}}{2}$, $\theta' = 1 - 2\theta$, and $\alpha = \frac{1-2\theta}{1-\theta}$, $\beta = 1 - \alpha$, the macro time step $t_n \rightarrow t_{n+1} = t_n + \Delta t$ is split into the three following consecutive substeps (with $\tilde{\theta} := \alpha\theta\Delta t = \beta\theta'\Delta t$):

$$
\begin{aligned}
[I+\tilde{\theta}N(\mathbf{v}^{n+\theta})]\mathbf{v}^{n+\theta}+\nabla p^{n+\theta} &= [I-\beta\theta\Delta tN(\mathbf{v}^{n})]\mathbf{v}^{n}+\theta\Delta t\mathbf{f}^{n}\\
\operatorname{div}\mathbf{v}^{n+\theta} &= 0\\
[I+\tilde{\theta}N(\mathbf{v}^{n+1-\theta})]\mathbf{v}^{n+1-\theta}+\nabla p^{n+1-\theta} &= [I-\alpha\theta'\Delta tN(\mathbf{v}^{n+\theta})]\mathbf{v}^{n+\theta}\\
&\quad +\theta'\Delta t\mathbf{f}^{n+1-\theta}\\
\operatorname{div}\mathbf{v}^{n+1-\theta} &= 0\\
[I+\tilde{\theta}N(\mathbf{v}^{n+1})]\mathbf{v}^{n+1}+\nabla p^{n+1} &= [I-\beta\theta\Delta tN(\mathbf{v}^{n+1-\theta})]\mathbf{v}^{n+1-\theta}\\
&\quad +\theta\Delta t\mathbf{f}^{n+1-\theta}\\
\operatorname{div}\mathbf{v}^{n+1} &= 0
\end{aligned}
$$

3.1.3 A modified Fractional-Step-θ-scheme

Consider an initial value problem of the following form, with $X(t)\in\mathbf{R}^d, d\geq 1$:

$$
\begin{cases}
\dfrac{dX}{dt} &= f(X,t) \quad \forall t>0\\
X(0) &= X_0
\end{cases}
\tag{22}
$$

Then, a modified θ-scheme (see [31]) with macro time step Δt can be written again as three consecutive substeps, where $\theta=1-1/\sqrt{2}$, $X^0=X_0$, $n\geq 0$ and X^n is known:

$$
\begin{aligned}
\frac{X^{n+\theta}-X^n}{\theta\Delta t} &= f\left(X^{n+\theta},t^{n+\theta}\right)\\
X^{n+1-\theta} &= \frac{1-\theta}{\theta}X^{n+\theta}+\frac{2\theta-1}{\theta}X^n\\
\frac{X^{n+1}-X^{n+1-\theta}}{\theta\Delta t} &= f\left(X^{n+1},t^{n+1}\right)
\end{aligned}
$$

As shown in [31], the 'classical' and the modified Fractional-Step-θ-schemes are

- fully implicit,
- strongly A-stable, and
- second order accurate (in fact, they are 'nearly' third order accurate [31]).

These important properties promise some advantageous behavior, particularly in implicit CFD simulations for nonstationary incompressible flow problems. Applying one step of this scheme to the Navier-Stokes equations, we obtain the following variant of the scheme:

$$1.\quad \begin{cases} \dfrac{\mathbf{v}^{n+\theta}-\mathbf{v}^{n}}{\theta\Delta t}+N(\mathbf{v}^{n+\theta})\mathbf{v}^{n+\theta}+\nabla p^{n+\theta}=\mathbf{f}^{n+\theta} \\ \operatorname{div}\mathbf{v}^{n+\theta}=0 \end{cases}$$

$$2.\quad \mathbf{v}^{n+1-\theta}=\tfrac{1-\theta}{\theta}\mathbf{v}^{n+\theta}+\tfrac{2\theta-1}{\theta}\mathbf{v}^{n}$$

$$3.\quad \begin{cases} \dfrac{\mathbf{v}^{n+1}-\mathbf{v}^{n+1-\theta}}{\theta\Delta t}+N(\mathbf{v}^{n+1})\mathbf{v}^{n+1}+\nabla \widetilde{p}^{n+1}=\mathbf{f}^{n+1} \\ \operatorname{div}\mathbf{v}^{n+1}=0 \end{cases}$$

$$3b.\quad p^{n+1}=(1-\theta)p^{n+\theta}+\theta\widetilde{p}^{n+1}$$

These 3 substeps build one macro time step and have to be compared with the previous description of the Backward Euler, Crank-Nicholson and the classical Fractional-Step-θ-scheme which all can be formulated in terms of a macro time step with 3 substeps, too. Then, the resulting accuracy and numerical cost are better comparable and the rating is fair. The main difference to the previous 'classical' Fractional-Step-θ-scheme is that substeps 1. and 3. look like a Backward Euler step while substep 2. is an extrapolation step only for previously computed data such that no operator evaluations at previous time steps are required.

Substep 3b. can be viewed as postprocessing step for updating the new pressure which however is not mandatory. In fact, in our numerical tests [31] we omitted this substep 3b. and accepted the pressure from substep 3. as final pressure approximation, that means $p^{n+1}=\widetilde{p}^{n+1}$.

Summarizing, the numerical effort of the modified scheme for each substep is cheaper at least for 'small' time steps (treatment of the nonlinearity) and complex right hand side evaluations, while the resulting accuracy is similar. The modified θ-scheme is a *Runge-Kutta* scheme; it has been derived in [12] as a particular case of the Fractional-Step-θ-scheme.

3.2 Solution algorithms

After applying the standard finite element method, the system of nonlinear algebraic equations arising from the governing equations described in subsection 2.1 and 2.2 reads (for incompressible solid material)

$$\begin{pmatrix} S_{\mathbf{uu}} & S_{\mathbf{uv}} & 0 \\ S_{\mathbf{vu}} & S_{\mathbf{vv}} & kB \\ c_{\mathbf{u}}B_s^T & c_{\mathbf{v}}B_f^T & 0 \end{pmatrix} \begin{pmatrix} \mathbf{u} \\ \mathbf{v} \\ p \end{pmatrix} = \begin{pmatrix} \mathbf{f}_{\mathbf{u}} \\ \mathbf{f}_{\mathbf{v}} \\ f_p \end{pmatrix}, \tag{23}$$

which is a typical saddle point problem, where S describes the diffusive and convective terms from the governing equations. The above system of nonlinear algebraic

equations (23) is solved using the Newton method as basic iteration which can exhibit quadratic convergence provided that the initial guess is sufficiently close to the solution. The basic idea of the Newton iteration is to find a root of a function, $\mathbf{R}(\mathbf{X}) = \mathbf{0}$, using the available known function value and its first derivative. One step of the Newton iteration can be written as

$$\mathbf{X}^{n+1} = \mathbf{X}^n + \omega^n \left[\frac{\partial \mathbf{R}(\mathbf{X^n})}{\partial \mathbf{X}} \right]^{-1} \mathbf{R}(\mathbf{X}^n), \tag{24}$$

where $\mathbf{X} = (\mathbf{u}_h, \mathbf{v}_h, p_h)$ and $\frac{\partial \mathbf{R}(\mathbf{X^n})}{\partial \mathbf{X}}$ is the Jacobian matrix. To ensure the convergence globally, some improvements of this basic iteration are used. The damped Newton method with line search improves the chance of convergence by adaptively changing the length of the correction vector (see [17, 29] for more details). The damping parameter $\omega^n \in (-1, 0)$ is chosen such that

$$\mathbf{R}(\mathbf{X}^{n+1}) \cdot \mathbf{X}^{n+1} \leq \mathbf{R}(\mathbf{X}^n) \cdot \mathbf{X}^n. \tag{25}$$

The damping greatly improves the robustness of the Newton iteration in the case when the current approximation $\mathbf{X}^n$ is not close enough to the final solution. The Jacobian matrix $\frac{\partial \mathbf{R}(\mathbf{X^n})}{\partial \mathbf{X}}$ can be computed by finite differences from the residual vector $\mathbf{R}(\mathbf{X})$

$$\left[\frac{\partial \mathbf{R}(\mathbf{X^n})}{\partial \mathbf{X}} \right]_{ij} \approx \frac{[\mathbf{R}]_i(\mathbf{X}^n + \alpha_j \mathbf{e}_j) - [\mathbf{R}]_i(\mathbf{X}^n - \alpha_j \mathbf{e}_j)}{2\alpha_j}, \tag{26}$$

where $\mathbf{e}_j$ are the unit basis vectors in $\mathbf{R}^n$ and the coefficients α_j are adaptively chosen according to the change in the solution in the previous time step. Since we know the sparsity pattern of the Jacobian matrix in advance, which is given by the used finite element method, this computation can be done in an efficient way such that the linear solver remains the dominant part in terms of the CPU time (see [29, 33]). A good candidate, at least in 2D, seems to be a direct solver for sparse systems like UMFPACK [8] or MUMPS [1]; while this choice provides very robust linear solvers, its memory and CPU time requirements are too high for larger systems (i.e. more than 20 000 unknowns). Large linear problems can be solved by Krylov-space methods (BiCGStab, GMRes [4]) with suitable preconditioners. One possibility is the ILU preconditioner with special treatment of the saddle point character of our system, where we allow certain fill-in for the zero diagonal blocks, see [6]. As an alternative, we also utilize a standard geometric multigrid approach based on a hierarchy of grids obtained by successive regular refinement of a given coarse mesh. The complete multigrid iteration is performed in the standard defect-correction setup with the V or F-type cycle. While a direct sparse solver [8] is used for the coarse grid solution, on finer levels a fixed number (2 or 4) of iterations by local MPSC schemes (Vanka-like smoother) [17, 29, 35] is performed. Such iterations can be written as

$$\begin{pmatrix} \mathbf{u}^{l+1} \\ \mathbf{v}^{l+1} \\ p^{l+1} \end{pmatrix} = \begin{pmatrix} \mathbf{u}^{l} \\ \mathbf{v}^{l} \\ p^{l} \end{pmatrix} - \omega \sum_{\text{element}\Omega_i} \begin{pmatrix} S_{\mathbf{uu}|\Omega_i} & S_{\mathbf{uv}|\Omega_i} & 0 \\ S_{\mathbf{vu}|\Omega_i} & S_{\mathbf{vv}|\Omega_i} & kB_{|\Omega_i} \\ c_{\mathbf{u}}B^T_{s|\Omega_i} & c_{\mathbf{v}}B^T_{f|\Omega_i} & 0 \end{pmatrix}^{-1} \begin{pmatrix} \mathbf{def}^l_{\mathbf{u}} \\ \mathbf{def}^l_{\mathbf{v}} \\ def^l_p \end{pmatrix}.$$

The inverse of the local (39×39) systems can be computed by hardware optimized direct solvers. The full nodal interpolation is used as the prolongation operator P with its transposed operator used as the restriction $\mathsf{R} = \mathsf{P}^T$, see [16, 29] for more details.

4 FSI benchmarking

In order to validate and to analyze different techniques to solve such FSI problems, also in a quantitative way, a set of benchmark configurations has been proposed in [30] (also see the contribution in this volume). The configurations consist of laminar incompressible channel flow around an elastic object which results in self-induced oscillations of the structure. Moreover, characteristic flow quantities and corresponding plots are provided for a quantitative comparison.

parameter	FSI1	FSI2	FSI3
ρ^s $[10^3 \frac{\text{kg}}{\text{m}^3}]$	1	10	1
ν^s	0.4	0.4	0.4
μ^s $[10^6 \frac{\text{kg}}{\text{ms}^2}]$	0.5	0.5	2.0
ρ^f $[10^3 \frac{\text{kg}}{\text{m}^3}]$	1	1	1
ν^f $[10^{-3} \frac{\text{m}^2}{\text{s}}]$	1	1	1
$\bar{U}$ $[\frac{\text{m}}{\text{s}}]$	0.2	1	2

parameter	FSI1	FSI2	FSI3
$\beta = \frac{\rho^s}{\rho^f}$	1	10	1
ν^s	0.4	0.4	0.4
$\text{Ae} = \frac{E^s}{\rho^f \bar{U}^2}$	3.5×10^4	1.4×10^3	1.4×10^3
$\text{Re} = \frac{\bar{U}d}{\nu^f}$	20	100	200
$\bar{U}$	0.2	1	2

Table 1 Parameter settings for the FSI benchmarks.

The domain is based on the 2D version of the well-known CFD benchmark in [32] and by omitting the elastic bar behind the cylinder one can easily recover the setup of the 'classical' *flow around cylinder* configuration which allows for validation of the flow part by comparing the results with the older flow benchmark. The setting is intentionally nonsymmetric to prevent the dependence of the onset of any possible oscillation on the precision of the computation. The mesh used for the computations is shown in Fig. 1. A parabolic velocity profile is prescribed at the left channel inflow

$$v^f(0,y) = 1.5\bar{U}\frac{y(H-y)}{\left(\frac{H}{2}\right)^2} = 1.5\bar{U}\frac{4.0}{0.1681}y(0.41-y), \tag{27}$$

such that the mean inflow velocity is $\bar{U}$ and the maximum of the inflow velocity profile is $1.5\bar{U}$. The *no-slip* condition is prescribed for the fluid on the other boundary parts. i.e. top and bottom wall, circle and fluid-structure interface Γ_t^0. The outflow condition can be chosen by the user, for example *stress free* or *do nothing* con-

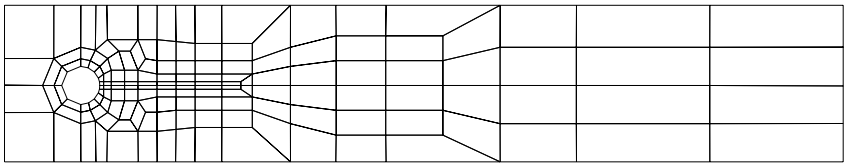

level	#refine	#el	#dof
0	0	62	1338
1	1	248	5032
2	2	992	19488
3	3	3968	76672
4	4	15872	304128
5	5	63488	1211392
6	6	253952	4835328
7	7	1015808	19320832

Fig. 1 Coarse mesh with number of degrees of freedom for refined levels.

ditions. The outflow condition effectively prescribes some reference value for the pressure variable p. While this value could be arbitrarily set in the incompressible case, in the case of compressible structure this will have influence on the stress and consequently the deformation of the solid. In this description, we set the reference pressure at the outflow to have *zero mean value*. Suggested starting procedure for the non-steady tests is to use a smooth increase of the velocity profile in time as

$$v^f(t,0,y) = \begin{cases} v^f(0,y)\frac{1-\cos(\frac{\pi}{2}t)}{2} & \text{if } t < 2.0 \\ v^f(0,y) & \text{otherwise} \end{cases} \tag{28}$$

where $v^f(0,y)$ is the velocity profile given in (27). The following FSI tests are performed for three different inflow speeds. FSI1 is resulting in a steady state solution, while FSI2 and FSI3 result in periodic solutions. The parameter values for the FSI1, FSI2 and FSI3 are given in the Table 1. Here, the computed values are summarized in Table 2 for the steady state test FSI1. In Figures 2 and 3, plots of the resulting x- and y-displacements of the trailing edge point A (see [30]) of the elastic bar and plots of the forces (lift, drag) acting on the cylinder and the bar are drawn. Furthermore, computed values for three different mesh refinement levels and two different time steps for the nonsteady tests FSI2 and FSI3 are presented respectively, which show the (almost) grid independent solution behavior (for more details see [30]).

5 FSI Optimization benchmarking

The objective of the following benchmarking scenario is to extend the validated FSI benchmark configurations towards optimization problems such that minimal drag/lift values of the elastic object, minimal pressure loss or minimal nonstationary oscillations through boundary control of the inflow, change of geometry or optimal

FSI2: x & y displacement of the point A [m].

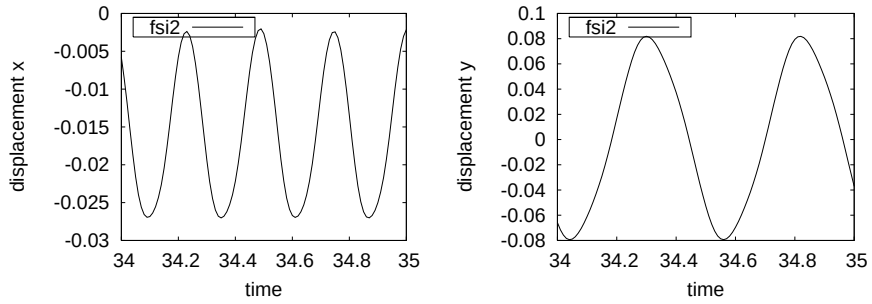

FSI2: lift and drag force [N] on the cylinder+elastic bar.

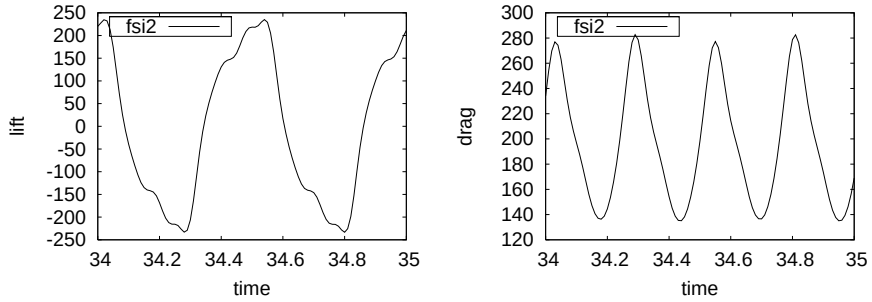

lev.	ux of A [$\times 10^{-3}$ m]	uy of A [$\times 10^{-3}$ m]	drag [N]	lift [N]
2	$-14.02 \pm 12.03[3.85]$	$1.25 \pm 79.3[1.93]$	$210.10 \pm 72.62[3.85]$	$0.25 \pm 227.9[1.93]$
3	$-14.54 \pm 12.50[3.86]$	$1.25 \pm 80.7[1.93]$	$212.83 \pm 75.89[3.86]$	$0.92 \pm 234.3[1.93]$
4	$-14.88 \pm 12.75[3.86]$	$1.24 \pm 81.7[1.93]$	$215.06 \pm 77.76[3.86]$	$0.82 \pm 237.1[1.93]$

lev.	ux of A [$\times 10^{-3}$ m]	uy of A [$\times 10^{-3}$ m]	drag [N]	lift [N]
2	$-14.01 \pm 12.04[3.86]$	$1.25 \pm 79.3[1.93]$	$210.09 \pm 72.82[3.86]$	$0.52 \pm 228.6[1.93]$
3	$-14.54 \pm 12.48[3.86]$	$1.25 \pm 80.7[1.93]$	$213.06 \pm 75.76[3.86]$	$0.85 \pm 234.4[1.93]$
4	$-14.87 \pm 12.73[3.86]$	$1.24 \pm 81.7[1.93]$	$215.18 \pm 77.78[3.86]$	$0.87 \pm 238.0[1.93]$

lev.	ux of A [$\times 10^{-3}$ m]	uy of A [$\times 10^{-3}$ m]	drag [N]	lift [N]
2	$-14.01 \pm 12.04[3.86]$	$1.28 \pm 79.2[1.93]$	$210.14 \pm 72.86[3.86]$	$0.49 \pm 228.7[1.93]$
3	$-14.48 \pm 12.45[3.86]$	$1.24 \pm 80.7[1.93]$	$213.05 \pm 75.74[3.86]$	$0.84 \pm 234.8[1.93]$
4	$-14.85 \pm 12.70[3.86]$	$1.30 \pm 81.6[1.93]$	$215.06 \pm 77.65[3.86]$	$0.61 \pm 237.8[1.93]$
ref.	$-14.85 \pm 12.70[3.86]$	$1.30 \pm 81.7[1.93]$	$215.06 \pm 77.65[3.86]$	$0.61 \pm 237.8[1.93]$

Fig. 2 Results for **FSI2** with time step $\Delta t = 0.002, \Delta t = 0.001, \Delta t = 0.0005$ [s].

FSI3: x & y displacement of the point A [m]

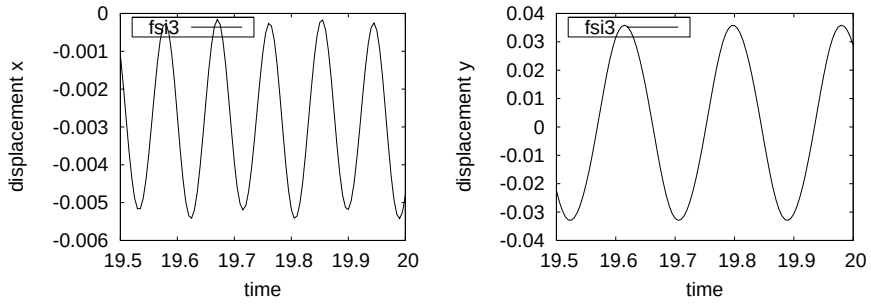

FSI3: lift and drag force [N] on the cylinder+elastic bar

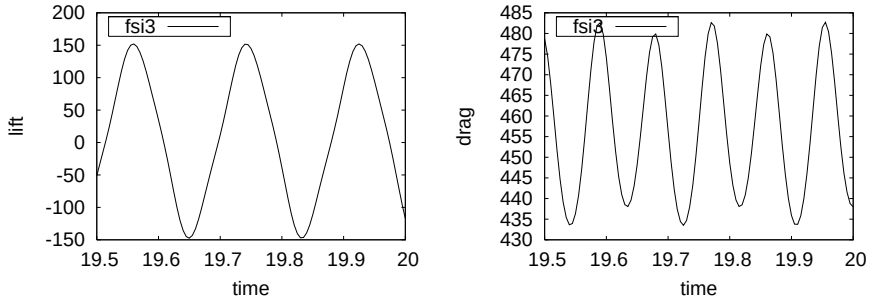

lev.	ux of A [$\times 10^{-3}$ m]	uy of A [$\times 10^{-3}$ m]	drag [N]	lift [N]
2	$-3.02 \pm 2.83[10.75]$	$1.41 \pm 35.47[5.37]$	$458.2 \pm 28.32[10.75]$	$2.41 \pm 145.58[5.37]$
3	$-2.78 \pm 2.62[10.93]$	$1.44 \pm 34.36[5.46]$	$459.1 \pm 26.63[10.93]$	$2.41 \pm 151.26[5.46]$
4	$-2.86 \pm 2.70[10.95]$	$1.45 \pm 34.93[5.47]$	$460.2 \pm 27.65[10.95]$	$2.47 \pm 154.87[5.47]$

lev.	ux of A [$\times 10^{-3}$ m]	uy of A [$\times 10^{-3}$ m]	drag [N]	lift [N]
2	$-3.02 \pm 2.85[10.75]$	$1.42 \pm 35.63[5.37]$	$458.7 \pm 28.78[10.75]$	$2.23 \pm 146.02[5.37]$
3	$-2.78 \pm 2.62[10.92]$	$1.44 \pm 34.35[5.46]$	$459.1 \pm 26.62[10.92]$	$2.39 \pm 150.68[5.46]$
4	$-2.86 \pm 2.70[10.92]$	$1.45 \pm 34.90[5.46]$	$460.2 \pm 27.47[10.92]$	$2.37 \pm 153.75[5.46]$

lev.	ux of A [$\times 10^{-3}$ m]	uy of A [$\times 10^{-3}$ m]	drag [N]	lift [N]
2	$-3.02 \pm 2.85[10.74]$	$1.32 \pm 35.73[5.36]$	$458.7 \pm 28.80[10.74]$	$2.23 \pm 146.00[5.36]$
3	$-2.77 \pm 2.61[10.93]$	$1.43 \pm 34.43[5.46]$	$459.1 \pm 26.50[10.93]$	$2.36 \pm 149.91[5.46]$
4	$-2.88 \pm 2.72[10.93]$	$1.47 \pm 34.99[5.46]$	$460.5 \pm 27.74[10.93]$	$2.50 \pm 153.91[5.46]$
ref.	$-2.88 \pm 2.72[10.93]$	$1.47 \pm 34.99[5.46]$	$460.5 \pm 27.74[10.93]$	$2.50 \pm 153.91[5.46]$

Fig. 3 Results for **FSI3** with time step $\Delta t = 0.001, \Delta t = 0.0005, \Delta t = 0.00025$ [s].

level	nel	ndof	ux of A [$\times 10^{-3}$ m]	uy of A [$\times 10^{-3}$ m]	drag [N]	lift [N]
2	992	19488	0.02287080	0.8193038	14.27359	0.7617550
3	3968	76672	0.02277423	0.8204231	14.29177	0.7630484
4	15872	304128	0.02273175	0.8207084	14.29484	0.7635608
5	63488	1211392	0.02271553	0.8208126	14.29486	0.7636992
6	253952	4835328	0.02270838	0.8208548	14.29451	0.7637359
7	1015808	19320832	0.02270493	0.8208773	14.29426	0.7637460
ref.			0.0227	0.8209	14.294	0.7637

Table 2 Results for **FSI1**.

control of volume forces can be achieved. The main design aim for the subsequent fluid structure interaction optimization problem is to minimize the lift on the beam with the help of boundary control of the inflow data. Here, the simulation is based on the described FSI1 configuration. Further extensions of this optimization problem will be to control minimal pressure loss or minimal nonstationary oscillations of the elastic beam through boundary control of the inflow section, change of the geometry (elastic channel walls or length/thickness of elastic beam) or optimal control of volume forces.

As described before, the position of the beam is not symmetric such that the lift is not zero. To minimize the lift value, we allow additional parabolic inflow at the top and additional parabolic outflow at the bottom of the domain. The location of the additional inlet and outlet is shown in the schematic diagram of the geometry in Figure 4. With V_1 and V_2 we denote the magnitude of the additional inflow and outflow velocity, respectively. Then, the aim is to

$$\begin{aligned} \text{minimize } & \left(\text{lift}^2 + \alpha(V_1^2 + V_2^2)\right) \\ \text{w.r.t. } & V_1, V_2. \end{aligned}$$

The arbitrary but fixed parameter $\alpha > 0$ reflects the 'costs' of the additional in- and outflow and has to be prescribed. The domain is based on the 2D version of the described FSI benchmark, shown in Figure 4; however, the thickness of the beam is increased from 0.02 to 0.04. Fluid and structural parameter values are based on the FSI1 benchmark. Table 3 provides an overview of the geometry parameters.

geometry parameters		value [m]
channel length	L	2.5
channel width	H	0.41
cylinder center position	C	$(0.2, 0.2)$
cylinder radius	r	0.05
elastic structure length	l	0.35
elastic structure thickness	h	0.04

Table 3 Overview of the geometry parameters.

Optimal points are those (V_1, V_2) values which result in minimal lift values on the beam depending on the parameter α. As α decreases we get the reduction of the lift

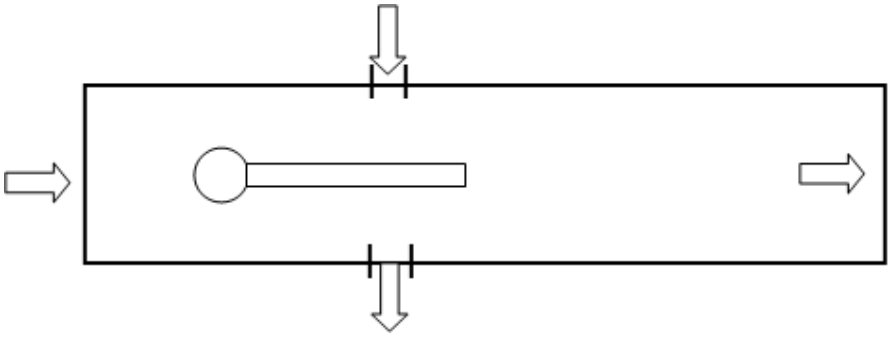

Fig. 4 Geometry and configuration of the problem.

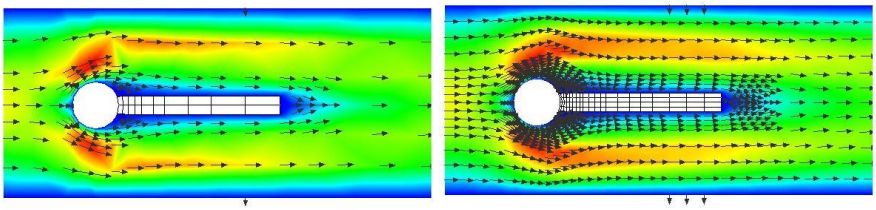

Fig. 5 No displacement is visible of the beam due to optimal boundary flow control: Level 1 (left), Level 2 (right).

	level 1			level 2		
α	iter	optimal values (V_1, V_2)	lift	iter	optimal values (V_1, V_2)	lift
1e+0	57	(3.74e-1, 3.88e-1)	8.1904e-1	59	(3.66e-1, 3.79e-1)	7.8497e-1
1e-2	60	(1.04e+0, 1.06e+0)	2.2684e-2	59	(1.02e+0, 1.04e+0)	2.1755e-2
1e-4	73	(1.06e+0, 1.08e+1)	2.3092e-4	71	(1.04e+0, 1.05e+01)	2.2147e-4
1e-6	81	(1.06e+0, 1.08e+1)	2.3096e-6	86	(1.04e+0, 1.05e+01)	2.2151e-6

Table 4 Results for FSI-Optimization.

on the beam, and the optimal values read $(1.06, 10.8)$ for level 1 and $(1.04, 10.5)$ for level 2 using the simplex algorithm proposed by Nelder and Mead [21]. Results are given in Table 4 which show the optimal values for the velocities V_1 and V_2 providing also the resulting lift on the beam as compared with the FSI1 benchmark values in Table 2. In Figure 5, it is visible that the displacement of the beam decreases with decreasing α, as well as the lift value decreases due to the boundary control. Keep in mind that the original lift on the beam is approximately 7.6e-1 for the FSI1 benchmark while in the case of FSI1-Optimization, it reduces to approximately 2.3e-6 for α=1e-6. Interested readers are referred to [18] for a comprehensive survey of the original Nelder-Mead simplex algorithm and for its advantages and disadvantages.

6 Applications to hemodynamics

In the following, we consider the numerical simulation of special problems encountered in the area of cardiovascular hemodynamics, namely flow interaction with thick-walled deformable material (here: the arterial walls) and rigid parts (here: stents), which can become a useful tool for deeper understanding of the onset of diseases of the human circulatory system, as for example blood cell and intimal damages in stenosis, aneurysm rupture, evaluation of new surgery techniques of the heart, arteries and veins (see [2, 19, 34] and the literature cited therein). In this contribution, prototypical studies are performed for brain aneurysms. The word 'aneurysm' comes from the latin word *aneurysma* which means dilatation. An aneurysm is a local dilatation in the wall of a blood vessel, usually an artery, due to a defect, disease or injury. Typically, as the aneurysm enlarges, the arterial wall becomes thinner and eventually leaks or ruptures, causing subarachnoid hemorrhage (SAH) (bleeding into brain fluid) or formation of a blood clot within the brain. In the case of a vessel rupture, there is a hemorrhage, which is particularly rapid and intense in case of an artery. In arteries the wall thickness can be up to 30% of the diameter and its local thickening can lead to the creation of an aneurysm. The aim of numerical simulations is to relate the aneurysm state (unrupture or rupture) with wall pressure, wall deformation and effective wall stress. Such a relationship would provide information for the diagnosis and treatment of unruptured and ruptured aneurysms by elucidating the risk of bleeding or rebleeding, respectively.

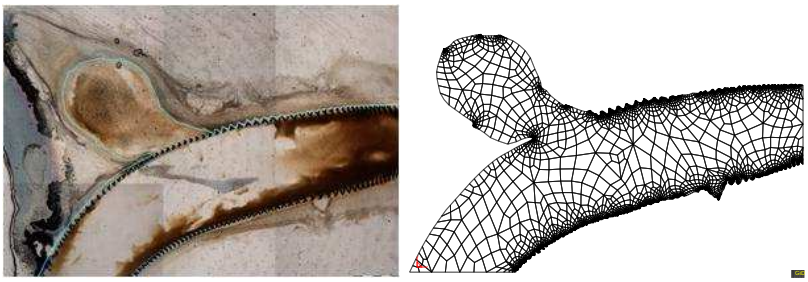

Fig. 6 Left: Real view of aneurysm. Right: Schematic drawing of the mesh.

As a typical example for the related CFD simulations, a real view is provided in Fig. 6 which also contains the automatically extracted computational domain and (coarse) mesh in 2D, however without stents. In order to use the proposed numerical methods for aneurysm hemodynamics, in a first step only simplified two-dimensional examples, which however include the interaction of the flow with the deformable material, are considered. Flow through a deformable vein with elastic walls of a brain aneurysm is simulated to analyze qualitatively the described methods; here, the flow is driven by prescribing the flow velocity at the inflow section (Poiseuille flow) while the solid part of the boundary is either fixed or stress-free. Both ends of

the walls are fixed, and the flow is driven by a periodical change of the inflow at the right end.

6.1 Geometry of the problem

For convenience, the geometry of the fluid domain under consideration is currently based on simplified 2D models, see Fig. 7, which allows to concentrate on the detailed qualitative evaluation of our approach based on the described monolithic ALE formulation. The underlying construction of the (2D) shape of the aneurysm can be explained as follows:

- The bent blood vessel is approximated by quarter circles around the origin.
- The innermost circle has the radius 6*mm*, the next has 8*mm*, and the last one has 8.25*mm*.
- This results in one rigid inner wall and an elastic wall between 8*mm* and 8.25*mm* of thickness 0.25*mm*.

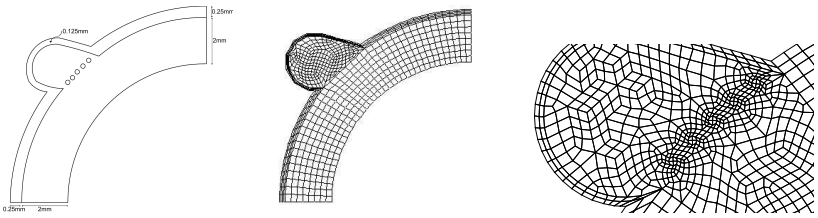

Fig. 7 Left: Schematic drawing of the measurement section. Middle: Mesh without stents (776 elements). Right: Mesh with stents (1431 elements) which are part of the simulations.

The aneurysm shape is approximated by two arcs and lines intersecting the arcs tangentially. The midpoints of the arcs are the same $(-6.75;6)$, they have the radius 1.125*mm* and 1.25*mm*. They are intersected tangentially by lines at angular value 1.3 radians. This results in a wall thickness of 0.125*mm* for the elastic aneurysm walls (see Fig. 7). The examined stents are of circular shape, placed on the neck of the aneurysm, and we use three, respectively five stents (simplified 'circles' in 2D as cutplanes from 3D configurations) of different size and position. Such stents (in real life) are typically used to keep arteries open and are located on the vessel wall while 'our' (2D) stent is located only near the aneurysm (Fig. 7). The purpose of this device is to reduce the flux into and within the aneurysm in order to occlude it by a clot or rupture.

6.2 Boundary and initial conditions

The (steady) velocity profile, to flow from the right to the left part of the channel, is defined as parabolic inflow, namely

$$\mathbf{v}^f(0,y) = \bar{U}(y-6)(y-8). \tag{29}$$

Correspondingly, the pulsatile inflow profile for the nonsteady tests for which peak systole and diastole occur for $\Delta t = 0.25s$ and $\Delta t = 0.75s$ respectively, is prescribed as

$$\mathbf{v}^f(t,0,y) = \mathbf{v}^f(0,y)(1+0.75sin(2\pi t)). \tag{30}$$

The natural outflow condition at the lower left part effectively prescribes some reference value for the pressure variable p, here $p = 0$. While this value could be arbitrarily set in the incompressible case, in the case of a compressible structure this might have influence on the stress and consequently the deformation of the solid. The *no-slip* condition is prescribed for the fluid on the other boundary parts, i.e. top and bottom wall, stents and fluid-structure interface.

6.3 Numerical results

The Newtonian fluid used in the tests has a density $\rho^f = 1.035 \times 10^{-6} kg/mm^3$ and a kinematic viscosity $\nu^f = 3.38 mm^2/s$ which is similar to the properties of blood. If we prescribe the inflow speed $\bar{U} = -50mm/s$, this results in a Reynolds number Re ≈ 120 based on the prescribed peak systole inflow velocity and the width of the veins which is $2mm$ such that the resulting flow is within the laminar region. Parameter values for the elastic vein in the described model are as follows: The density of the upper elastic wall is $\rho^s = 1.12 \times 10^{-6} kg/mm^3$, solid shear modulus is $\mu^s = 42.85 kg/mms^2$, Poisson ratio is $\nu^s = 0.4$, Young modulus is $E = 120 kN/mm^2$. As described before, the constitutive relations used for the materials are the incompressible Newtonian model (2) for the fluid and a hyperelastic Neo-Hooke material for the solid. This choice includes most of the typical difficulties the numerical method has to deal with, namely the incompressibility and significant deformations.

From a medical point of view, the use of stents provides an efficient treatment for managing the difficult entity of intracranial aneurysms. Here, the thickness of the aneurysm wall is attenuated and the aneurysm hemodynamics changes significantly. Since the purpose of this device is to control the flux within the aneurysm in order to occlude it by a clot or rupture, the resulting flow behavior into and within the aneurysm is the main objective, particularly in view of the different stent geometries. Therefore, we decided for the 2D studies to locate the stents only in direct connection to the aneurysm.

Comparing our studies with the CFD literature (see [2, 9, 27, 28, 34]), several research groups focus on CFD simulations with realistic 3D geometries, but typi-

cally assuming rigid walls. In contrast, we concentrate on the complex interaction between elastic deformations and flow perturbations induced by the stents. At the moment, we are only able to perform these simulations in 2D. However, with these studies we should be able to analyze qualitatively the influence of geometrical details onto the elastic material behavior, particularly in view of more complex blood models and constitutive equations for the structure. Therefore, the aims of our current studies can be described as follows:

1. What is the influence of the elasticity of the walls onto the flow behavior inside the aneurysm, particularly w.r.t. the resulting shape of the aneurysm?
2. What is the influence of the geometrical details of the (2D) stents, that means shape, size, position, on the flow into and inside the aneurysm?
3. Do both aspects, small-scale geometrical details as well as elastic fluid-structure interaction, have to be considered simultaneously or is one of them negligible in first order approximation?
4. Are modern numerical methods and corresponding CFD simulation tools able to simulate qualitatively the multiphysics behavior of such biomedical configurations?

In the following, we show some corresponding results for the described prototypical aneurysm geometry, first for the steady state inflow profile, followed by nonsteady tests for the pulsatile inflow, both with rigid and elastic walls, respectively.

6.3.1 Steady configurations

Due to the given inflow profile, which is not time-dependent, and due to the low Reynolds numbers, the flow behavior leads to a steady state which only depends on the elasticity and the shape of the stents. Moreover, for the following simulations, we only treat the aneurysm wall as elastic structure. Then, the aneurysm undergoes some slight deformations which can hardly be seen in the following figures. However, they result in a different volume of the flow domain (see Fig. 9) and lead to a significantly different local flow behavior since the spacing between stents and elastic walls may change (see Figure 8).

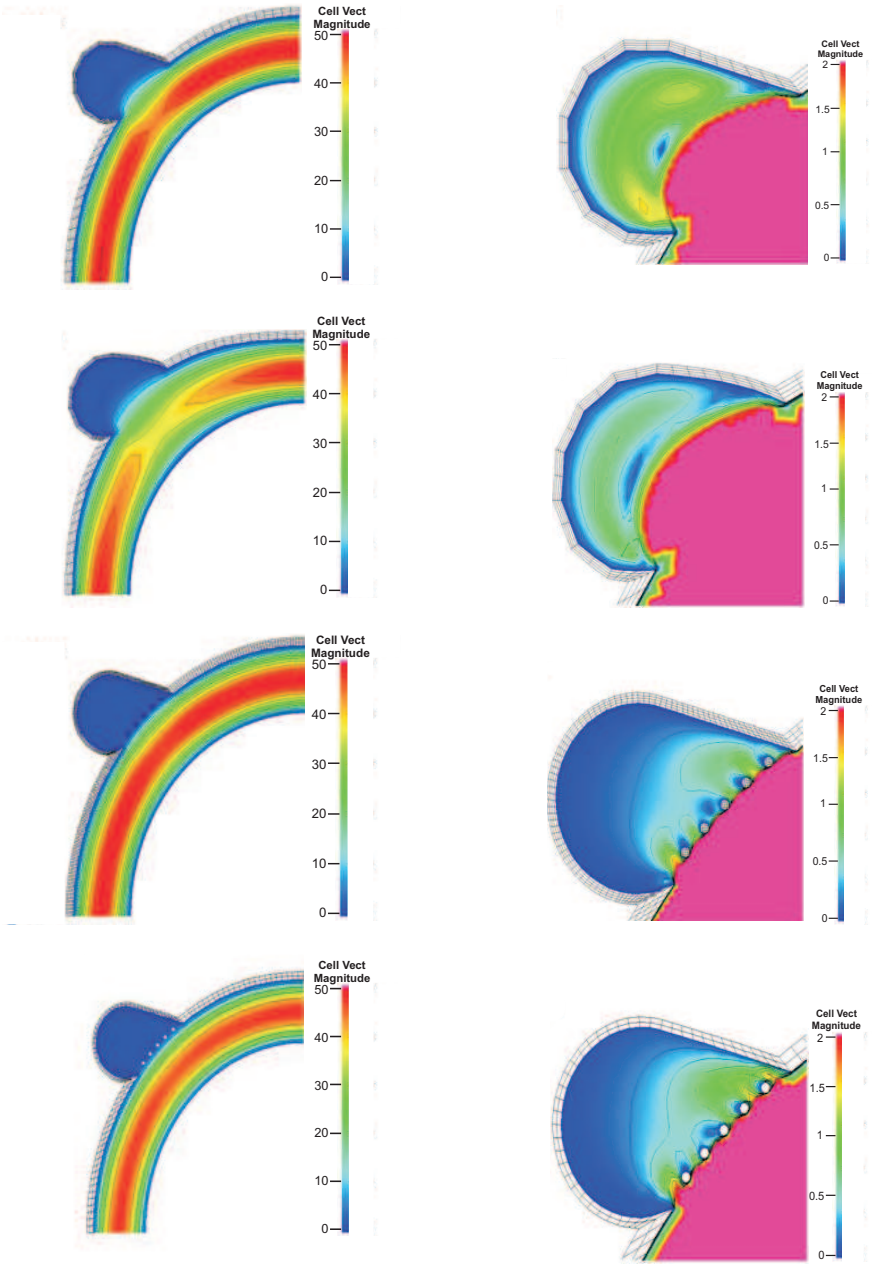

Fig. 8 Magnitude of the blood flow velocity for four configurations. Top to bottom: Rigid walls without stents, elastic walls without stents, rigid walls with stents, elastic walls with stents. Left: Overall view. Right: Scaled view of the aneurysm.

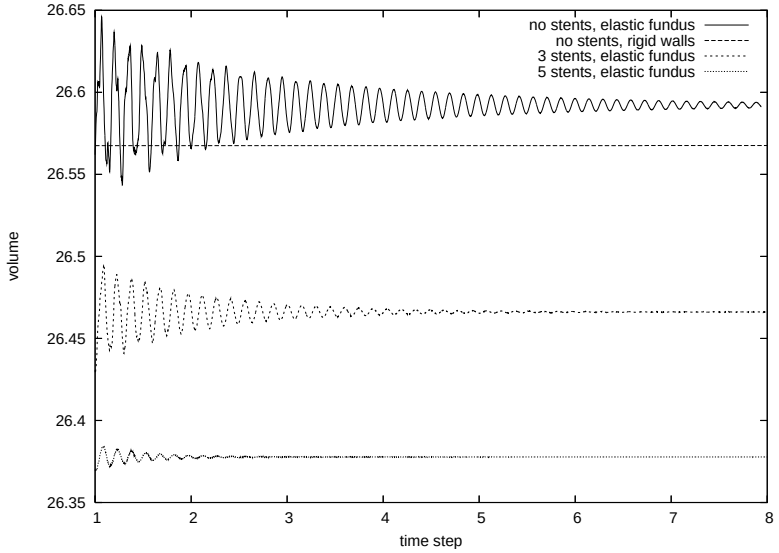

Fig. 9 Resulting volume of the fluid domain for different configurations.

In Figure 11, we visualize the different flow behavior by coloring corresponding to the velocity magnitude and by showing corresponding vector plots inside the aneurysm. Particularly the influence of the number of stents on the complete fluid flow through the channel including the aneurysm can be clearly seen.

Summarizing these results for steady inflow, the simulations show that the stent implantation across the neck of the aneurysm prevents blood penetration into the aneurysm fundus. Moreover, the elastic geometrical deformation of the wall is slightly reduced by implanting the stents while the local flow behavior inside the aneurysm is more significantly influenced by the elastic properties of the outer wall, particularly due to different width between stents and walls of the aneurysm. In the next section, we will consider the behaviour of more realistic flow configurations with time-dependent pulsatile inflow which will be analyzed for the case of elastic behaviour of the aneurysm walls.

6.3.2 Pulsatile configurations

For the following pulsatile test case, we have taken again the aneurysm part as elastic while the other parts of the walls belonging to the channel are rigid. First of all, we show again (see Fig. 10) the resulting volume of the flow domain for five, three and no stents. In all cases, the oscillating behavior due to the pulsatile inflow is visible which also leads to different volume sizes. Looking carefully at the resulting flow behavior, we see differences w.r.t. the channel flow near the aneurysm, namely due

to the different flow rate into the aneurysm, and significant local differences inside the aneurysm.

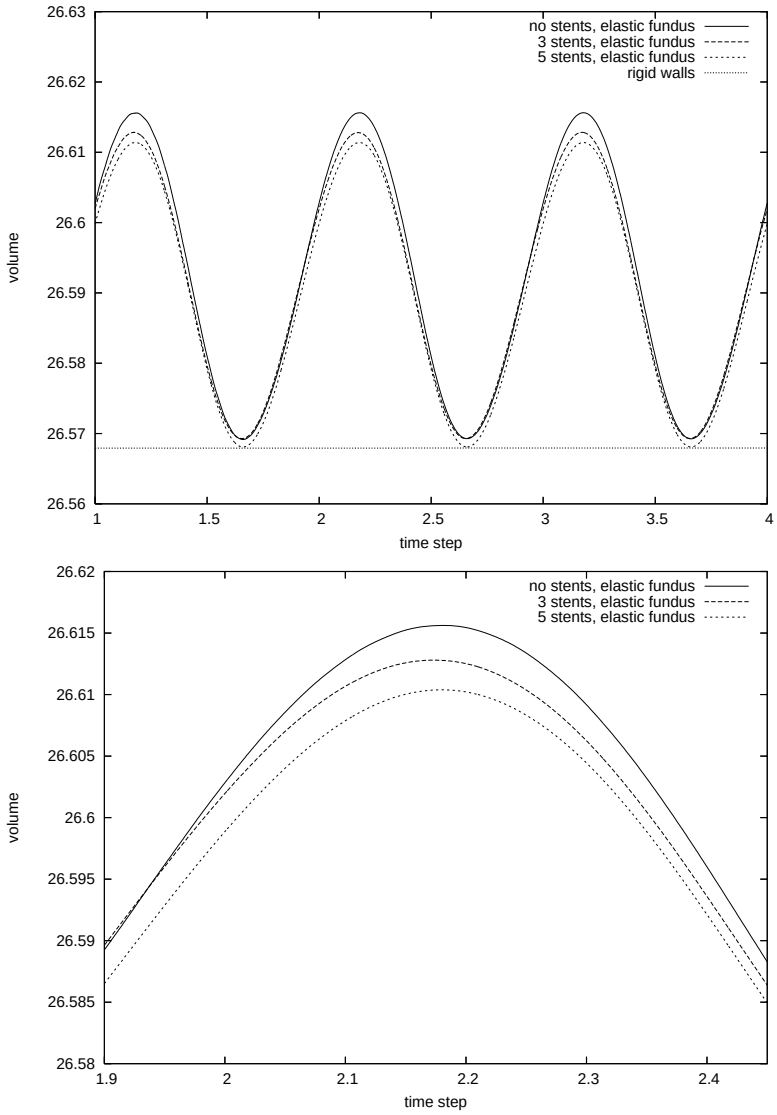

Fig. 10 Domain volume with rigid and elastic behavior of the aneurysm wall.

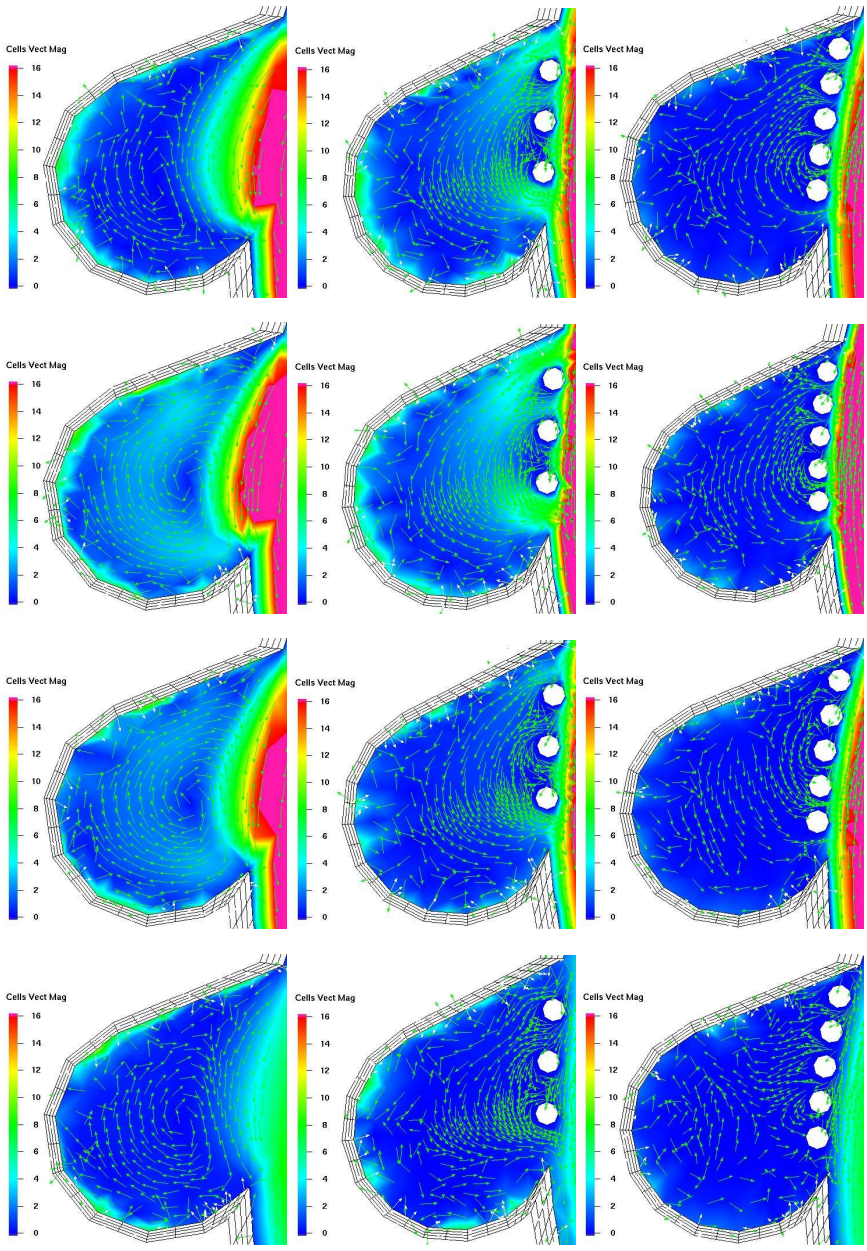

Fig. 11 Left column: no stent. Middle column: three stents. Right column: five stents. Figures demonstrate the local behavior of the fluid flow inside the aneurysm during one cycle.

6.3.3 Extension to 3D

Finally, we show first results of extending the monolithic formulation to 3D. A similar problem of pulsatile flow in an elastic tube with an aneurysm-like cavity is solved. The material parameters are the same as in the previous section and the resulting deformation and flow field at different times are shown in Figure 12.

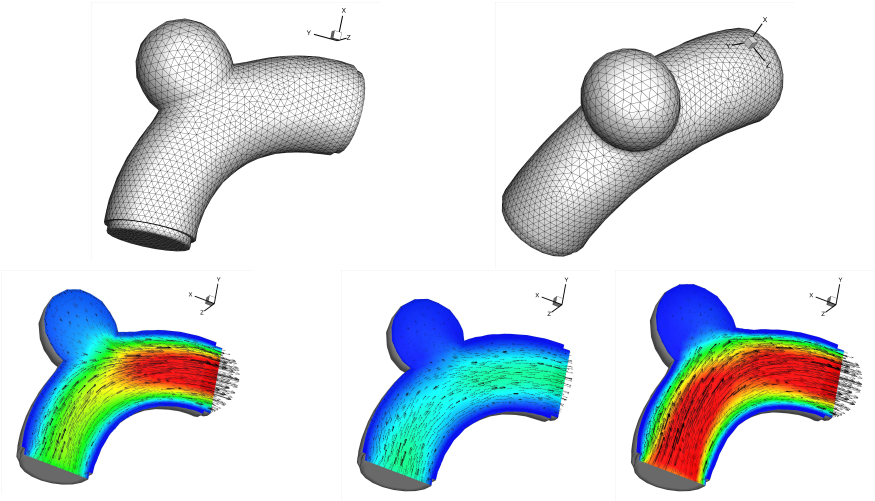

Fig. 12 Pulsatile fluid flow through an elastic tube with cavity. Flow field represented by velocity vectors and velocity magnitude at different times.

7 Summary and future developments

We presented a monolithic ALE formulation of fluid-structure interaction problems suitable for applications with large structural deformations and laminar viscous flows, particularly arising in biomechanics. The corresponding discrete nonlinear systems result from the finite element discretization by using the high order Q_2P_1 FEM pair. The systems are solved monolithically via a discrete Newton iteration and special Krylov-multigrid approaches.

While we restricted our studies to the simplified case of Newtonian fluids and small deformations, the used numerical components allow the system to be coupled with additional models of chemical and electric activation of the active response of the biological material as well as power law models used to describe the shear thinning property of blood. Further extension to viscoelastic models and coupling with mixture based models for soft tissues together with chemical and electric processes allow to perform more realistic simulations for real applications.

We applied the presented numerical techniques to FSI benchmarking settings ('channel flow around cylinder with attached elastic beam', see [30]) which allow the validation and also evaluation of different numerical solution approaches for fluid-structure interaction problems. Moreover, we examined prototypically the influence of endovascular stent implantation on aneurysm hemodynamics. The aim was, first of all, to study the influence of the elasticity of the walls on the flow behavior inside the aneurysm. Moreover, different geometrical configurations of implanted stent structures have been analyzed in 2D. These 2D results are far from providing quantitative results for such a complex multiphysics configuration, but they allow a qualitative analysis w.r.t. both considered components, namely the elastic behavior of the structural parts and the multiscale flow behavior due to the geometrical details of the stents. We believe that such basic studies are helpful for the development of future 'Virtual Flow Laboratories' which individually assist to design personal medical tools.

Acknowledegment:
The authors want to express their gratitude to the German Research Association (DFG), funding the project as part of FOR493 and TRR30, the Jindřich Nečas Center for Mathematical Modeling, project LC06052 financed by MSMT, and the Higher Education Commission (HEC) of Pakistan for their financial support of the study. The present material is also based upon work kindly supported by the Homburger Forschungsförderungsprogramm (HOMFOR) 2008.

References

[1] P. R. Amestoy, I. S. Duff, and J. Y. L'Excellent. Multifrontal parallel distributed symmetric and unsymmetric solvers. *Computer Methods in Applied Mechanics and Engineering*, 184(2-4):501 – 520, 2000.

[2] S. Appanaboyina, F. Mut, R. Löhner, E. Scrivano, C. Miranda, P. Lylyk, C. Putman, and J. Cebral. Computational modelling of blood flow in side arterial branches after stenting of cerebral aneurysm. *International Journal of Computational Fluid Dynamics*, 22:669–676, 2008.

[3] D. N. Arnold, D. Boffi, and R. S. Falk. Approximation by quadrilateral finite element. *Math. Comput.*, 71:909–922, 2002.

[4] R. Barrett, M. Berry, T. F. Chan, J. Demmel, J. Donato, J. Dongarra, V. Eijkhout, R. Pozo, C. Romine, and H. Van der Vorst. *Templates for the solution of linear systems: Building blocks for iterative methods*. SIAM, Philadelphia, PA, second edition, 1994.

[5] D. Boffi and L.. Gastaldi. On the quadrilateral Q_2P_1 element for the Stokes problem. *Int. J. Numer. Meth. Fluids.*, 39:1001–1011, 2002.

[6] R. Bramley and X. Wang. *SPLIB: A library of iterative methods for sparse linear systems*. Department of Computer Science, Indiana University, Bloom-

ington, IN, 1997. http://www.cs.indiana.edu/ftp/bramley/splib.tar.gz.

[7] H. Damanik, J. Hron, A. Ouazzi, and S. Turek. A monolithic FEM approach for non-isothermal incompressible viscous flows. *Journal of Computational Physics*, 228:3869–3881, 2009.

[8] T. A. Davis and I. S. Duff. A combined unifrontal/multifrontal method for unsymmetric sparse matrices. *ACM Trans. Math. Software*, 25(1):1–19, 1999.

[9] M. A. Fernandez, J-F. Gerbeau, and V. Martin. Numerical simulation of blood flows through a porous interface. *ESAIM: Mathematical Modelling and Numerical Analysis*, 42:961–990, 2008.

[10] M. Fortin. Old and new finite elements for incompressible flows. *International Journal for Numerical Methods in Fluids*, 1(4), 1981.

[11] Y. C. Fung. *Biomechanics: Mechanical Properties of Living Tissues.* Springer-Verlag, New York, 1993.

[12] R. Glowinski. Finite element method for incompressible viscous flow. In P. G Ciarlet and J. L. Lions, editors, *Handbook of Numerical Analysis*, Volume IX,, pages 3–1176. North-Holland, Amsterdam, 2003.

[13] P. M. Gresho. On the theory of semi-implicit projection methods for viscous incompressible flow and its implementation via a finite element method that also introduces a nearly consistent mass matrix, part 1: Theory. *Int. J. Numer. Meth. Fluids.*, 11:587–620, 1990.

[14] G. A. Holzapfel. *A continuum approach for engineering.* John Wiley and Sons, Chichester, UK, 2000.

[15] G. A. Holzapfel. Determination of meterial models for arterial walls from uni-axial extension tests and histological structure. *International Journal for Numerical Methods in Fluids*, 238(2):290–302, 2006.

[16] J. Hron, A. Ouazzi, and S. Turek. A computational comparison of two FEM solvers for nonlinear incompressible flow. In E. Bänsch, editor, *Challenges in Scientific Computing*, LNCSE:53, pages 87–109. Springer, 2002.

[17] J. Hron and S. Turek. A monolithic FEM/multigrid solver for ALE formulation of fluid structure interaction with application in biomechanics. In H.-J. Bungartz and M. Schäfer, editors, *Fluid-Structure Interaction: Modelling, Simulation, Optimisation*, LNCSE:53. Springer, 2006.

[18] J. C. Lagarias, J. A. Reeds, M. H. Wright, and P. E. Wright. Convergence properties of the Nelder-Mead simplex method in low dimensions. *SIAM J. Optim.*, 9:112–147, 1998.

[19] R. Löhner, J. Cebral, and S. Appanaboyina. Parabolic recovery of boundary gradients. *Communications in Numerical Methods in Engineering*, 24:1611–1615, 2008.

[20] D. A. McDonald. Blood flow in arteries. In *second ed.* Edward Arnold, 1974.

[21] J. A. Nelder and R. Mead. A simplex method for function minimization. *Computer Journal*, 7(4):308–313, 1965.

[22] R. Rannacher and S. Turek. A simple nonconforming quadrilateral Stokes element. *Numer. Methods Partial Differential Equations.*, 8:97–111, 1992.

[23] M. Razzaq. *Numerical techniques for solving fluid-structure interaction problems with applications to bio-engineering*. PhD Thesis, TU Dortmund, to appear, 2010.

[24] M. Razzaq, J. Hron, and S. Turek. Numerical simulation of laminar incompressible fluid-structure interaction for elastic material with point constraints. In R. Rannacher and A. Sequeira, editors, *Advances in Mathematical Fluid Mechancis-Dedicated to Giovanni paolo Galdi on the Occasion of his 60th Birthday*. Springer, in print, 2009.

[25] T. E. Tezduyar, S. Sathe, T. Cragin, B. Nanna, B.S. Conklin, J. Pausewang, and M. Schwaab. Modeling of fluid structure interactions with the space time finite elements: Arterial fluid mechanics. *International Journal for Numerical Methods in Fluids*, 54:901–922, 2007.

[26] T. E. Tezduyar, S. Sathe, M. Schwaab, and B.S. Conklin. Arterial fluid mechanics modeling with the stabilized space time fluid structure interaction technique. *International Journal for Numerical Methods in Fluids*, 57:601–629, 2008.

[27] R. Torri, M. Oshima, T. Kobayashi, K. Takagi, and T.E. Tezduyar. Influence of wall elasticity in patient-specific hemodynamic simulations. *Computers and Fluids*, 36:160–168, 2007.

[28] R. Torri, M. Oshima, T. Kobayashi, K. Takagi, and T.E. Tezduyar. Numerical investigation of the effect of hypertensive blood pressure on cerebral aneurysm dependence of the effect on the aneurysm shape. *International Journal for Numerical Methods in Fluids*, 54:995–1009, 2007.

[29] S. Turek. *Efficient Solvers for Incompressible Flow Problems: An Algorithmic and Computational Approach*. Springer-Verlag, 1999.

[30] S. Turek and J. Hron. Proposal for numerical benchmarking of fluid-structure interaction between an elastic object and laminar incompressible flow. In H.-J. Bungartz and M. Schäfer, editors, *Fluid-Structure Interaction: Modelling, Simulation, Optimisation*, LNCSE:53. Springer, 2006.

[31] S. Turek, L. Rivkind, J. Hron, and R. Glowinski. Numerical study of a modified time-steeping theta-scheme for incompressible flow simulations. *Journal of Scientific Computing*, 28:533–547, 2006.

[32] S. Turek and M. Schäfer. Benchmark computations of laminar flow around cylinder. In E.H. Hirschel, editor, *Flow Simulation with High-Performance Computers II*, volume 52 of *Notes on Numerical Fluid Mechanics*. Vieweg, 1996. co. F. Durst, E. Krause, R. Rannacher.

[33] S. Turek and R. Schmachtel. Fully coupled and operator-splitting approaches for natural convection flows in enclosures. *International Journal for Numerical Methods in Fluids*, 40:1109–1119, 2002.

[34] A. Valencia, D. Ladermann, R. Rivera, E. Bravo, and M. Galvez. Blood flow dynamics and fluid–structure interaction in patient-specific bifurcating cerebral aneurysms. *International Journal for Numerical Methods in Fluids*, 58:1081–1100, 2008.

[35] S. P. Vanka. Implicit multigrid solutions of Navier-Stokes equations in primitive variables. *J. of Comp. Phys.*, 65:138–158, 1985.